
Proceedings Paper:
Urwick, A.N., Bastianini, F., Pérez, G.E. et al. (1 more author) (2022) Deciphering perovskite decomposition in a humid atmosphere with TOF-GISANS. In: McNeilly, T., (ed.) Energy Reports. 6th Annual CDT Conference in Energy Storage and Its Applications, 05-06 Apr 2022, Sheffield, UK. Elsevier , pp. 23-33.

https://doi.org/10.1016/j.egyr.2022.05.044

Available online at www.sciencedirect.com
ScienceDirect
Energy Reports 8 (2022) 23–33
www.elsevier.com/locate/egyr

6th Annual Centre for Doctoral Training Conference in Energy Storage and Its Applications, 2022

Deciphering perovskite decomposition in a humid atmosphere with TOF-GISANS

Adam N. Urwick[a,*], Francesco Bastianini[b], Gabriel E. Pérez[c], Alan Dunbar[a]

[a] *Department of Chemical and Biological Engineering, University of Sheffield, Sheffield S1 3JD, UK*
[b] *SmartKem Ltd, Manchester Technology Center, Hexagon Tower, Delaunays Road, Blackley, Manchester, M9 8GQ, UK*
[c] *Neutron and Muon Source, Science and Technology Facilities Council, Rutherford Appleton Laboratory, Didcot, OX11 0QX3, UK*

Received 9 May 2022; accepted 13 May 2022
Available online xxxx

Abstract

Doping or alloying of the cations on the A-site and halides on the X site of ABX_3 perovskites has been demonstrated as a successful technique for improving moisture stability of perovskite films for optoelectronic applications. Despite structural and electrical stability improvements, these films still undergo moisture induced degradation to Lead Iodide and other photo-inactive phases, reducing device lifetime and performance. Understanding of their moisture induced degradation has been limited by the contrast mechanisms and sensitivity of optical and x-ray scattering techniques. Time-of-Flight Grazing Incidence Small Angle Neutron Scattering (TOF-GISANS) presents itself as a powerful alternative capable of identifying low atomic weight phases and offering depth resolution. Herein we use TOF-GISANS to begin to uncover moisture induced degradation pathways in various mixed perovskite systems fabricated under ambient conditions and exposed to 90% rH in the dark for up to 12 h, showing poor stoichiometric homogeneity through the bulk of the film and facile formation of deuterated by-products at ambient temperatures. We find evidence indicative of formation of PbI_2, and $PbBr_2$ from peaks apparent in scattering from the surface of $MAPbI_3$, $FA_{0.83}MA_{0.17}Pb(I_{0.83}Br_{0.17})_3$, and $FA_{0.83}Cs_{0.17}Pb(I_{0.83}Br_{0.17})_3$ thin films, with degradation less pronounced in the latter films containing Cs. Deuterated by-products form readily, resulting in decreasing average particle size as perovskite crystals swell and fragment from the grain periphery inwards. $Cs_{0.05}(FA_{0.83}MA_{0.17})_{0.95}Pb(I_{0.84}Br_{0.16})_3$ shows impressive phase resilience compared to the other mixtures, with minimal segregation to other phases observed in vertical cuts through the 2D scattering image, though still exhibits deleterious morphological degradation. TOF-GISANS is demonstrated as a powerful tool for characterisation of these materials, with significant potential for future investigations into phase changes in thin films.

Peer-review under responsibility of the scientific committee of the 6th Annual Centre for Doctoral Training Conference in Energy Storage and Its Applications, 2022.

Keywords: Perovskite; Grazing incidence; Small Angle Neutron Scattering; Scattering length density; Doping; Moisture stability. Degradation

* Corresponding author.
E-mail address: aurwick1@sheffield.ac.uk (A.N. Urwick).

https://doi.org/10.1016/j.egyr.2022.05.044

Peer-review under responsibility of the scientific committee of the 6th Annual Centre for Doctoral Training Conference in Energy Storage and Its Applications, 2022.

1. Introduction

Moisture induced degradation of perovskites is responsible for performance reduction over device lifetimes. The aristotypical $MAPbI_3$ is particularly susceptible to moisture due to the crystal cell parameters permitting facile penetration by water molecules, resulting in the formation of intermediary monohydrate and dihydrated perovskite phases [1]. H_2O molecules form strong H-bonds with organic cations, weakening the bond between the cation and octahedral Pb ion. This enables rapid deprotonation of the A-site cation and leaves the perovskite vulnerable to other exogenous degradation factors [2,3]. H_2O reacts with Iodide, creating hydroiodic acid, methylamine and PbI_2 [4]. Liao et al. performed nanoscale mapping of the humidity induced degradation of polycrystalline $MAPbI_3$ films treated with Ethyl Acetate antisolvent at 90% relative humidity (rH). Their findings suggest that the reaction proceeds initially through humidity induced grain growth and atomic rearrangement, followed by formation of a monohydrate layer which, due to its low stability at room temperature, degrades to PbI_2 through the evaporation of Methylammonium Iodide (MAI) and H_2O. Moisture continues to diffuse through the semi-amorphous hydrated grain boundaries repeating this process, and these grain boundaries are the last surfaces to develop PbI_2. PbI_2 eventually covers surfaces and grain boundaries, limiting further moisture ingress, or loss of the metastable hydrated phase [5]. Similarly, Wang et al. reported the susceptibility of an amorphous region at the perovskite grain boundary to react with moisture, finding it to have a much higher propensity to react than the grain surface. They link this to the higher proportion of defects at the grain boundary allowing H_2O to permeate into the bulk and initiate degradation [6]. This resonates with reports of perovskite stoichiometry being initially preserved at the surface while PbI_2 is produced in the bulk and at grain boundaries by [7].

The reaction of $MAPbI_3$ and H_2O to form the monohydrate $MAPbI_3{\cdot}H_20$ has been shown to be reversible, whereas the subsequent reaction to form the dihydrate phase $(CH_3NH_3)_4PbI_6{\cdot}$ 2H2O is irreversible, and characterised by the loss of volatile MA^+, HI, I_2, NH_3 and the production of PbI_2. In a time resolved X-ray diffraction (XRD) study under 70% rH, Leguy et al. found this pathway proceeded trough the loss of MAI [8]. Evidence for the hydrate and PbI_2 formation was also found in an in-situ grazing incidence XRD (GIXRD) study at 100% rH of moisture induced degradation by Yang et al. and Petrus et al. using in-situ XRD (75% rH), as well as in the in-operando XRD study at 50% rH by Schelhas et al. [9–11]. Exposure of $MAPbI_3$ solar cells to rH $>$ 50% rapidly deteriorates device performances [12]. Schlipf et al. used Grazing Incidence Small Angle Neutron Scattering (GISANS) to analyse the water content, degradation products, and morphological changes of $MAPbI_3$ films during prolonged exposure to humidity (D_2O) [13]. Under high rH, metastable hydrate phases form as the faceted crystals are transformed to rounded ones. The films incorporated more water than is simply integrated into the hydrates, with smaller crystals more strongly affected. Even at low humidity water is adsorbed on the surfaces of crystal domains. Above 93% rH the dihydrate phase forms. The uptake of water and formation of hydrates is accompanied by swelling of the grains. Moisture induced degradation has also been observed in encapsulated devices: Chu et al. found that in polymethyl methacrylate (PMMA) coated films with micrometre sized $MAPbI_3$ grains at 35% rH over 6 days, moisture diffusion through the PMMA layer leads to the fragmentation of grains, and this disintegration was not centred on grain boundaries [14].

Tuning the perovskite structure by X-site and A-site substitution to enhance the interaction between the A-site cations and Pb ion reduces the lattice cell parameters. This ensures the crystal retains the perovskite crystal structure upon extended moisture exposure. Replacing the MA^+ cations with less acidic cations such as FA^+ ($CH(NH2)2^+$) or Cs^+ also reduces deprotonation and stabilises the perovskite lattice [1,15]. Substitution of MA^+ with FA^+ has been investigated due to a favourable band gap and greater thermal and photo-stability [16,17]. Black photo-active α-$FAPbI_3$ is thermodynamically unstable below 150 °C, converting to a yellow non-perovskite hexagonal phase δ-$FAPbI_3$ at room temperature. [18] Due to inherent volatility of the MA^+ cation the mixed $MA_XFA_{1-x}PbI_3$ perovskite has been further stabilised by addition of Cs^+ by various researchers, or the removal of MA^+ in favour of a Cs^+ component [15][19–21]. A-site doping with Cs^+ has been show to increase moisture, thermal, and photo-stability in $FA_{1-x}Cs_xPbI_3$, $FA_{1-x}Cs_xPbI_{1-y}Br_y$ and $Cs_x(FA_{0.83}MA_{0.17})_{100-x}Pb(I_{0.83}Br_{0.17})_3)_{0.95}$ [22,23]. The small ionic radius of Cs^+ (1.67 Å) in contrast to FA^+ (2.53 Å) and MA^+ (2.16 Å) improves bonding between the organic cation and $[PbI_6]^{2-}$ octahedra [15]. It also prevents I^- migration, a crucial factor in device instability.[16] The lattice parameter can be further tuned by halide substitution of I^- with Br^-. There is a linear relationship between the Br content and the lattice parameters of $MAPbI_{3-x}Br_x$ phases, with a tetragonal–cubic transition between $x = 0.13$ and 0.20 [12].

While these strategies are effective in reducing degradation, a performance reduction persists even in encapsulated devices over hundreds of hours of illumination under dry conditions. There have been many contributions to understanding the degradation routes in some mixed cation perovskite films. Ho et al. found that under light and high relative humidity, $FA_{0.85}Cs_{0.15}PbI_3$ degradation follows a multistage pathway [24]. In the first stage between 0-11 h, PbI_2 rich depressions form as FAI evaporates. The mixed cation phase separates into $CsPbI_3$ needles and large $FAPbI_3$ grains. Degradation stops for a couple hours, before proceeding in the second stage with the shrinking of $FAPbI_3$ grain. However, at 85% rH In the dark, depressions are not formed, and instead large grains develop after 80 h exposure. This suggests a different pathway in the dark. Similarly, Li et al. identify photo-inactive, current blocking Cs-rich clusters after ageing $FA_{0.9}Cs_{0.1}PbI_3$ under operating conditions [25]. Maniyarasu et al. investigated the moisture degradation of $FA_{1-x}Cs_xPbI_3$ at 30% rH. Using photoelectron spectroscopy, they found that Cs was depleted from the surface alongside the organic cations. While the FACs based perovskite stabilised with Rb shows a ratio of Cs to Pb close to nominal, for FACs the Cs/Pb ratio is about half the nominal concentration at the highest depth probe, reducing towards the surface. XPS also suggests the surface is easily depleted of alkali cations due to decomposition of the perovskite lattice [26]. Addition of RbI fills iodine vacancies and stabilises the perovskite, and it is possible that triple cation, FA-MA-Cs compositions may have a similar response. Hu et al. looked at triple cation perovskites at 75% rH in the dark using XRD and after exposure to 90% rH using energy dispersive X-ray spectroscopy (EDX). According to XRD, there was minor degradation of $FA_{0.83}MA_{0.17}Pb(I_{0.83}Br_{0.17})_3$ and $Cs_{0.05}FA_{0.83}MA_{0.17}Pb(I_{0.83}Br_{0.17})_3$ to PbI_2 after 1 h exposure. After 5 days exposure at 90% rH they found moisture induced phase segregation and degradation in 5% Cs doped $FA_{0.83}MA_{0.17}Pb(I_{0.83}Br_{0.17})_3$. The degraded region of the film had a Cs and Br rich phase identified as $CsPb_2I_4Br$ [27]. Interestingly they do not find a change in the elemental stoichiometry of FAMA or phase segregation after 90% rH exposure for 2 days.

By using broad neutron wavelengths, GISANS geometry and Time-of-Flight (TOF) detectors to investigate both surface and bulk characteristics of perovskite films, we compare the moisture induced degradation in the dark of perovskite films with differing A-site cation combinations and comparable X-site halide mixtures to $MAPbI_3$. TOF-GISANS was demonstrated by Wolff et al. in their depth-resolved study of block co-polymer micelles close to the surface of silicon substrates [28]. We find, true to form, that $Cs_{0.05}(FA_{0.83}MA_{0.17})_{0.95}Pb(I_{0.84}Br_{0.16})_3$ shows the least degradation. We show the production of PbI_2, $PbBr_2$, and deuterated perovskite phases to varying degrees in each sample as well as evidence for the production of $CsPb_2I_4Br$ and various deuterated phases by comparing peaks in the SANS profiles with calculated values for scattering length density, b. A mixture of Cs, FA and MA on the A site and I and Br on the X-site lead to a film with enhanced moisture stability compared to $FA_{0.83}MA_{0.17}Pb(I_{0.83}Br_{0.17})_3$ or MAPbI3 films, and this is likely due to the stabilisation of the perovskite α-phase. This agrees with literature reports of greater thermodynamic stability in perovskite films engineered to be structurally closer to the ideal cubic phase [15,23,29,30]. Importantly we also find the more rapid decline in characteristic length-scales of mesoscale scattering features in the bulk as opposed to at the surface, and the morphological degradation being accentuated at the grain periphery, leading to a decrease in average particle size. This complements the previously cited evidence that degradation proceeds in the bulk as opposed to at the surface of the film, and suggests that the grain decomposes cyclically as material at the periphery is exposed to moisture, eventually leading to fragmentation of the grain.

2. Theory

In this work we investigate the moisture resilience of $MAPbI_3$, $FA_{0.83}MA_{0.17}Pb(I_{0.83}Br_{0.17})_3$, $Cs_{0.05}(FA_{0.83}MA_{0.17})_{0.95}Pb(I_{0.84}Br_{0.16})_3$, and $FA_{0.83}Cs_{0.17}Pb(I_{0.83}Br_{0.17})_3$; hereafter MAPI, FAMAX, CsFAMAX, and FACsX using a combination of GISANS and scanning electron microscopy (SEM). Grazing incidence small angle neutron scattering (GISANS) as a technique is sensitive to the morphology as well as the alignment of lateral and vertical structures at a nanometre scale [31–33]. It utilises concepts from grazing incidence diffraction, small angle scattering, and reflectometry to explore scattering from the sample in all directions, generally utilising an area detector. Grazing incidence geometries typically exploit incident beam angles (θ_i) below the critical angle (θ_c) of the thin film (the angle below which perfect reflections of the incident beam will occur) which causes the imaginary component of the incident beam to spread out along the surface, allowing interrogation of a large scattering volume. Above θ_c, the neutron beam penetrates deeply into the bulk. Hence surface or near-surface and bulk film structures can be inspected separately by changing the incident angle. The penetration depth varies with the wavelength of the incident beam, meaning depth sensitivity can also be varied by changing the incident wavelength (λ) around a single optimised incident angle.

In this paper we use broad neutron wavelengths in combination with Time-of-Flight (TOF) detectors to investigate both surface and bulk characteristics of perovskite films. For each wavelength within the band a scattering data set is obtained simultaneously. Providing the gap between pulses is long enough to prevent overlap, then as the initial position and velocity of the neutrons is known, measuring the final position on the detector and the time to reach it allow neutrons of different wavelength to be assigned. Hence neutrons which have elastically scattered according to the Bragg condition should reach the detector before neutrons which scatter in an inelastic fashion, and as different features will satisfy this condition at different wavelengths, all that needs to be done to investigate different features is the selection of the appropriate wavelength within the band.

The combination of reflected and refracted waves due to interaction with the sample will produce a 2D image on the beam detector. The horizon line splits the 2D image into the transmitted and reflected beam contributions. Taking a horizontal or vertical cut through the 2D image at a fixed exit angle will give different information on the structures related to those intensity measurements. At the small angles used in GISANS, the 2D detector mostly probes the q_y and q_z"- contributions, as q_x is very small due to the solid angle probed on the Ewald sphere being small, and therefore curvature is negligible. Small values of $q_{y"-}$ correlate with larger structures, so a horizontal cut gives information on distribution and relative proportion of lateral structural features at differing length scales depending on the q_y value. Mesoscale structures of interest at small values of q_y can be identified from scattering features which result from the periodic distribution of structures on the nanoscale, arising from Bragg-like scattering in diffraction. A vertical cut (q_z) will give information in vertical changes in structure, such as those occurring at the interface between laminar layers of materials, and phase changes through the bulk of the film.

Contrast arises from interactions between incident neutrons and nuclei or unpaired electrons. The strength of these interactions dictates the amplitude of the scattered neutron wave, and is measured using the scattering length density (b). b is determined experimentally and its variation from one isotope to another can be utilised in isotopic labelling to investigate structures. Herein we use a D_2O atmosphere to characterise the uptake of moisture by perovskite films. As D_2O displaces organic cations and deuterated phases form, the different b of the corresponding phases will produce scattering peaks on the GISANS detector, emerging from the perovskite and revealing their position over time relative to the phases containing nominally intrinsic H isotopes. H has a negative b (-3.739) whereas D has a positive b (6.671).

GISANS experiments were carried out at Sans2d at the ISIS neutron source to investigate the uptake of moisture in different perovskite films. The high flux and wide q range enable the characterisation of particles as small as 0.5 nm. The analysis investigates the extent of degradation in terms of changing particle size (swelling due to uptake and adsorption of moisture in perovskite crystals) and due to degradation (to perovskite components such as the constituent salts and hydrated phases). Performing the experiment in the dark allows us to eliminate the contribution of UV induced degradation of perovskite to Lead Halides [34]. Herein we use GISANS to analyse both the phase evolution and characteristic distances in different perovskite chemistries. Scattering data is plotted using Kratky plots of (Ixq^2) vs. q. This normalises scattering profiles by mass and concentration reducing the scattering intensity decay and making features more obvious. We model horizontal cuts through a 2D scattering intensity image from a neutron band of 8–12.5 Å (using TOF analysis we optimise the incident beam at 8 Å) using a simplistic sphere model in SasView to estimate the characteristic length-scales associated with mesoscale features on the order of hundreds of nanometres. Similarly, horizontal cuts of scattering data induced by a 3.8 Å incident beam are used to interrogate particle dimensions at the surface of the films. We use scattering peaks from vertical cuts from a band of 3.8–4.2 Å in combination with calculated b's for predicted degradation products of the various perovskites to determine the evolved state of the film moisture exposure. Vertical cuts from scattering patterns induced by an 8 Åbeam chiefly show scattering above the critical angle, allowing reflectometry-like diffraction experiments. The shape of the reflectometry profile provides structural information such as density thickness and roughness. Modelling this has been outside the scope of this paper but demonstrates the depth of information that can be obtained from this characterisation technique in a single measurement.

3. Materials and methods

For GISANS experiments, perovskites were prepared according to the stoichiometries previously described. They were dissolved in a solution of DMF:DMSO in volumetric ratio of 4:1, and stirred for at least an hour at room temperature prior to deposition. The Silicon substrates were cleaned prior to deposition by polishing the deposition surface, and sequentially rinsing with acetone and 2-propanol. Before deposition of perovskite the Si wafer surface

was functionalised with O_2 plasma treatment. 100 μl of perovskite solution was dripped on 5 cm wide, 4 mm thick Silicon Wafer substrates and spun at 3000 rpm for 30 s in a fume cupboard with an rH of 30% and ambient temperature of 20 °C. Si has a small absorption cross-section and negligibly scatters neutrons, reducing interference with measurements. The perovskite films were annealed on a hotplate at 100 °C for 30 min and then transferred to the humidity chamber containing an LiCl salt solution, which maintains rH at ∼25%. After the first measurement in LiCl (0 h), the salt solution was swapped for an NaCl solution, which raised humidity to ∼90% and the hydration measurements were taken. It took approximately 20 min to reach rh ∼80% and 100 min to reach rH ∼90%. The maximum beam diameter was 15 mm.

3.1. Experimental methods

An in-situ degradation study of perovskite films upon exposure to a relative humidity of 90% levels was done using GISANS. Degradation of thin films is associated with hydrated phases moisture, change in particle size and q-scale. The experimental setup for these in-situ measurements is shown in Fig. 1. Precursor solutions were made up and were spun on cleaned Si wafers. Samples were placed in a humidity chamber containing saturated salt solution baths and an Arduino connected hygrometer which was linked to a laptop. The chamber was provided by ISIS, while the humidity measurement system was devised in-house (hygrometer + Arduino code and laptop control). The chamber had neutron-transparent windows, facilitating in-situ GISANS measurements of the film as moisture is adsorbed on the surface and chemical and morphological changes occur. Salt solutions of NaCl were used to attain a relative humidity of 90%, while LiCl was used to dry the experimental chamber, and create a constant base humidity of approximately 25%. The Arduino-hygrometer detector setup saturated in the ISIS experiment, necessitating a reference measurement to be taken in the Sheffield laboratory. The issue of humidity measurement was resolved with measured humidity as per expectations from review of humidity control in the laboratory using Salt Solutions by Young [35]. Scanning Electron microscopy images were obtained using a JSM-6010LA (JEOL) with an accelerating voltage of 15 kV and working distance of 10 mm. Analysis of images was done using ImageJ [36]. Images (Mx200) underwent the following processing: 3D Gaussian Blur, 3D Median, Threshold tool (to convert to binary 8 bit image), Erosion or dilation to better define grain boundaries, and Analyse Particles (Overlay) to obtain a list of particle sizes.

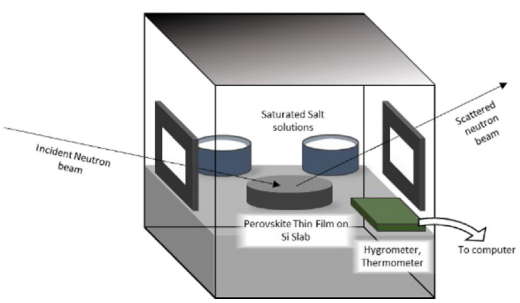

Fig. 1. Small Angle Neutron Scattering experiment setup for in-situ moisture degradation.

4. Results and discussion

The raw GISANS at the selected incident wavelengths can be partitioned into vertical and horizontal components. Fig. 2(a) shows neutron reflectometry-like specular reflectance from a vertical cut of scattering of an 8 Åincident beam. The experimental approach used in this paper provides this data from which laminar thickness can be determined. A full analysis of these extracts from the data falls outside the scope of this work. Fig. 2(b) shows the degradation of $MAPbI_3$ during moisture exposure to Lead Iodide (q ∼0.016Å^{-1}) and $MAPbI_3$ mono and dideuterates (0.018 Å^{-1} and 0.014 Å^{-1}) respectively. The horizontal cut in Fig. 2(c) at 8 Å shows the increasing scattering intensity over time as a result of moisture induced grain boundary reorientation and particle fragmentation throughout the bulk of the film both decreasing average particle size (q increasing) and increases the concentration of particles around a characteristic length scale, which changes over time as per Fig. 2(d). The sphere model of particle size based on horizontal cut measurements as per Fig. 2(c) over time show that the characteristic length-scale R

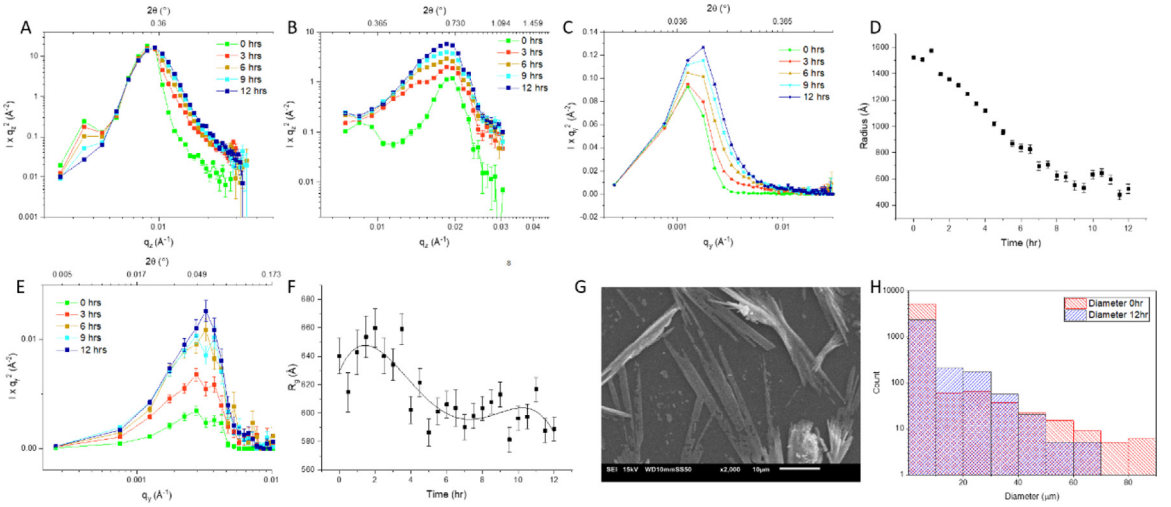

Fig. 2. A, B, C, E; Kratky Plots of $MAPbI_3$ films over the duration of 90% rH exposure. 0 h refers to films in an LiCl solution controlled atmosphere with rH∼25%. A: A vertical cut through a 2D image from scattering from an incidence neutron beam with λ of 8 Å (cut 'at' 8 Å for shorthand) showing the diffuse reflection peak (Yoneda Peak), where the off-specular scattering peak coincides with the specular peak ($\theta_f = \theta_c$). B: A vertical cut at 3.8 Å. C: A horizontal cut at 8 Å. D. A sphere model fit of particles based on scattering from horizontal cuts at 8 Å. E: Horizontal cut at 3.8 Å. F: Guinier model fit of particles based on scattering in E. G: SEM image at Mx2000 after 8 h exposure to moisture.

decreases from ∼1600 Å to ∼500 Å(50 nm) over 12 h. This implies the typical distance between particles reducing as large grains fragment into smaller granules. Fig. 2(e) depicts horizontal cuts at 3.8 Å showing the reducing particle size at the surface of the film (q shifts right), and the consolidation of particles in two size regimes around a shared mean after 12 h. Fig. 2(f) uses a Guinier model to fit the measurements as per Fig. 2(e) over time. Larger error bars are due to poorer sensitivity of this SANS experiment at these length-scales (10s of nm). The guide-for-the-eye polynomial fitted to the scatter plot suggests a size fluctuation in particle size at the surface, although there is a negative trend over time. The first hour sees an increase in particle size due to the uptake of moisture and formation of PbI_2 and mono-deuterated perovskites. Thereafter particle size decreases—perovskite degrades to the di-deuterate phase. Around 9 h we also see a small peak above the background from $Pb(OH_2)$ ($q = 0.028$ Å^{-1}), and PbO ($q = 0.024$ Å^{-1}). Contrasting Fig. 1(f) and Fig. 1(d), it appears that the characteristic length-scales (correlated with particle size) are diminishing more rapidly in the bulk than at the surface, which corroborates with previous findings by Chen et al. of moisture induced decomposition resulting first in the production of PbI_2 in the bulk of the film, and preservation of perovskite stoichiometry at the surface [7]. The SEM image (Fig. 2(g)) of $MAPbI_3$ after 8 h exposure to moisture shows the degradation of the tetragonal spherulitic particles too smaller crystallites. The histogram (Fig. 2(h)) comparing the particle size distribution before (0 h) and after exposure to rH 90% (12 h) finds that hydration has the effect of both reducing the number of particles <10 μm and >70 μm in diameter. This is in agreement with the observation from Fig. 2(e) of a narrowing of the particle size distribution. $MAPbI_3$ follows the degradation pathway identified by previous researchers, though it is noticeable that we also see formation of $Pb(OH_2)$ and PbO after extended exposure [8,37–39].

According to Fig. 3(a), Initially the FAMAX film shows a peak centred on $q = 0.019$ Å^{-1}, which is a convolution of FAMAX (q∼0.017 Å^{-1}) and $PbBr_2$ (q∼0.02 Å^{-1}). There is also a broad left shoulder centred on q∼0.014 Å^{-1}, from $FAPbI_3$ (0.014 Å^{-1}) and a slight shoulder on the right. This shows poor homogeneity of the film stoichiometry post-annealing. The right shoulder at q∼0.022 Å^{-1} grows after 2 h, coinciding with $FAPbBr_3$-mono-deuterate (q∼0.023 Å^{-1}), $MAPbBr_3$ mono-deuterate (q∼0.021 Å^{-1}), and the FAMAX-mono-deuterate phase (q∼0.021 Å^{-1}). After 2 h, the left shoulder has also sharpened into a second defined peak, likely due to increased production of PbI_2 (q∼0.015 Å^{-1}). At 4 h a peak in $PbBr_2$ (q∼0.019 Å^{-1}) is produced as well. After 10 h the left peak centre has increased in height and shifted rightwards, likely due to degradation of FAMAX to PbI_2 and $FAPbI_3$. It is likely the broadening of the right peak is also due to deuteration of the $FAPbI_3$ degradation product to $FAPbI_3$-monodeuterate

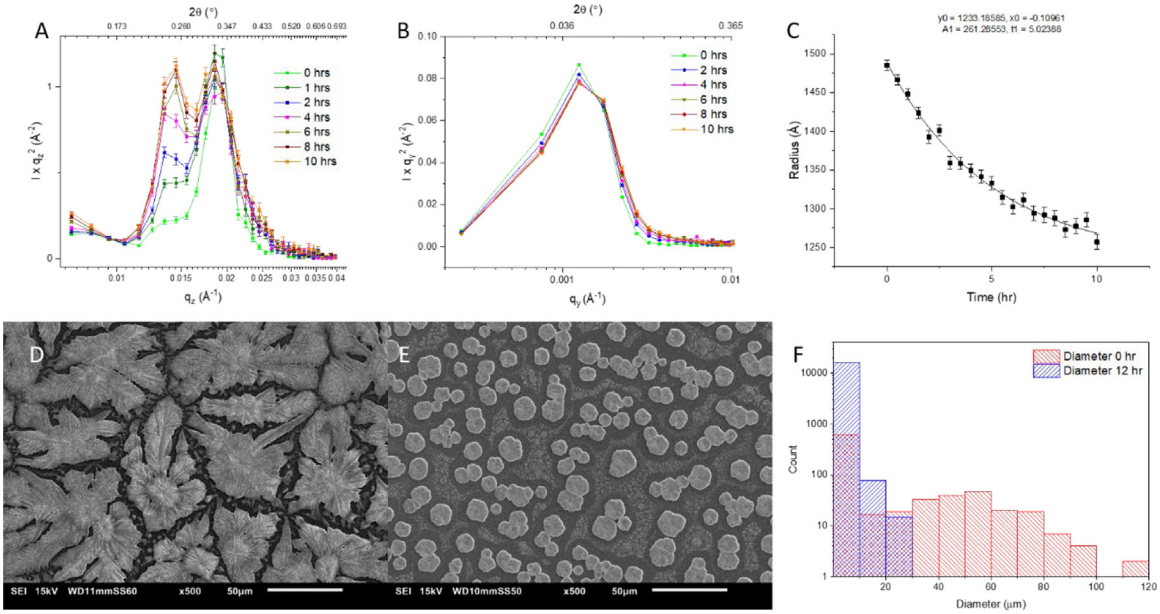

Fig. 3. A, B; Kratky plots of FAMAX films over time at 90% rH. A: A Vertical Cut at 3.8 Å showing the degradation of FAMA. B: A horizontal cut at 8 Å showing small rightwards peak shift. C: A sphere model of the particles as per the scattering from B. D: SEM images of FAMAX film before and (E) after (8 h) exposure to moisture. F: Particle size distribution before and after (12 h) hydration.

(q∼0.02 Å^{-1}) and di-deuterate (q∼0.019 Å^{-1}), and possibly FAMAX-di-deuterate (q∼0.018 Å^{-1}). There is no strong contribution from $MAPbI_3$ (q∼0.01 Å^{-1}) although a leftward shift of the right peak centre may indicate formation of $MAPbBr_3$ (q∼0.016 Å^{-1}) or $FAPbBr_3$. It has previously been shown that $MAPbBr_3$ is significantly more stable than $MAPbI_3$, so we may be seeing loss of MAI from $MAPbI_3$ to form PbI_2 and $MAPbI_3$-deuterates whereas $MAPbBr_3$ is retained or converted to deuterated by-products [40]. After 10 h, we also begin to see small peaks (above background) at q∼0.28 Å^{-1} and q∼0.24 Å^{-1}, due to production of $PbOH_2$ and PbO. The horizontal cut at 8 Å (Fig. 3(b)) shows the scattering peak shifts to the right and decreases slightly in intensity. This suggests decreasing particle size and also reducing crystalline order. This is supported by Fig. 3(c): a sphere model of the scattering as per Fig. 3(b), with the characteristic length-scale (radius on the y-axis) decreasing steeply over the course of the experiment. If we compare SEM images in Fig. 3(d-e) before and after 8 h exposure to moisture, we see significant deterioration of the initially defined grains to a mixture of rounded, smaller grains similar to the core structures at the centre of the larger initial grains, and smaller crystallites occupying the space between. Comparing the distribution of particle sizes in Fig. 3(f), we see the absence of grains above 30 μm after moisture exposure, in contrast to the broad spread prior with some grains larger than 100 μm.

At 0 h in Fig. 4(a) of FACsX vertically integrated scattering at 3.8 Å, there are two prominent peaks—the left peak arises from $FAPbI_3$, at q∼0.138 Å^{-1}, while the right peak from FACsX at q∼0.0185 Å^{-1} and a contribution from $FAPbI_3$-mono-deuterate. There is also a small shoulder around q∼0.0225 Å^{-1}, which may relate to $FAPbBr_3$-mono-deuterate or FACsX-mono-deuterate (q∼0.0215 Å^{-1}). This once again exposes poor stoichiometric heterogeneity through the bulk of the film after film formation in ambient conditions. After 8 h, we see a peak at q∼0.0145 Å^{-1}, which corresponds with the previously identified $CsPb_2I_4Br$. (q∼0.014 Å^{-1}) in degrading $Cs_{0.05}FA_{0.83}MA_{0.17}Pb(I_{0.83}Br_{0.17})_3$ [27]. We also see increased scattering intensity peaking at q∼0.0195 Å^{-1}, which may relate to $PbBr_2$ production (q∼0.0195 Å^{-1}). There is a small peak at q∼0.0285 Å^{-1}, which relates to $PbOH_2$. After 10 h, the valley between the two peaks has risen, reducing the prominence of the peaks. This indicates production of PbI_2 (q∼0.0156 Å^{-1}). The shift of the left peak to lower q implicates the degradation of FACsX to $FAPbI_3$. The broad right peak is a convolution of $FAPbI_3$ and $FAPbBr_3$ deuterates, FACsX, and FACsX-deuterates, resulting in the much larger peak intensity after hydration. In Fig. 4(b), a horizontal cut at 8 Åshows very slight scattering increase at higher q (∼0.03 Å^{-1}) over time, suggesting decreasing particle size. The sphere model fit of the data in Fig. 4(c) as per scattering in Fig. 4(b) shows this relates to a decrease in the characteristic radius,

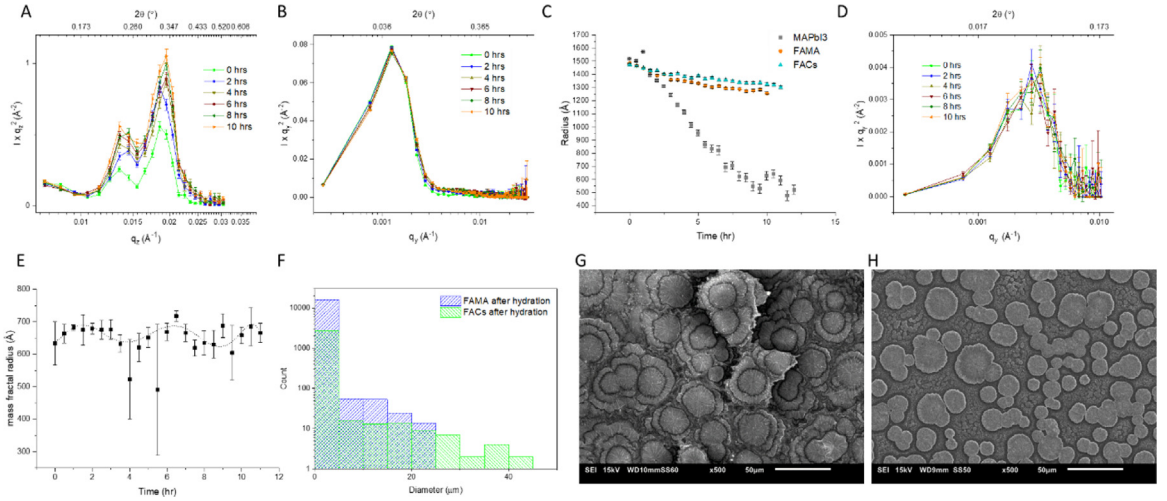

Fig. 4. A, B, D; Kratky Plots of FACsX; (A) A vertical cut at 3.8 Å showing degradation of FACsX over 10 h. (B) A horizontal cut at 8 Å showing a slight increase in scattering around $q = 0.003$. (C) Sphere model fit of horizontal cut scattering as per B, showing decrease in characteristic radius. (D) Horizontal cut at 3.8 Å. (E) Mass fractal model fit of horizontal cut scattering as per D, with dashed line providing guide for the eye. (E) Particle Size distribution between FAMAX and FACsX after hydration. (F–G) SEM images of FACsX before and after hydration (Mx500).

decreasing by ∼150 Å. As the figure shows, this is an improvement over both compositions containing MAI. Taking a horizontal cut at 3.8 Å (Fig. 4(d)) shows less variation at the surface of the film. Modelling this scattering using a mass-fractal model shows a fluctuation in characteristic length-scales. This suggests the surface is quite dynamic during moisture exposure, with an ebb and flow of material between subsumption by larger particles and degradation (indicated by guide-for-the-eye dashed line). The resilient surface may also tie-in with the observation as per $MAPbI_3$ of bulk concentrated degradation as moisture percolates through grain boundaries and surfaces into the core of the film and degrades perovskite to PbI_2 and deuterated/hydrated phases. Morphology shown in the SEM image show the film has undergone similar decomposition to the FAMAX film, with two size regimes; grains between 10–50 µm and granules on the scale of 100s of nm–5 µm. Degradation is less pronounced, with the particle distribution histogram Fig. 4(d) comparing particles in FACsX and FAMAX after moisture exposure for 8 h showing larger grains present, and fewer grains < 5 µm.

Fig. 5(a) of a 3.8 Å horizontal cut of CsFAMA shows moisture exposure decreases the particle size of some surface features, with increased intensity at q∼0.045 $Å^{-1}$. After 3 h, particle size degradation is expressed as two shoulders at q∼0.018 $Å^{-1}$ and 0.04 $Å^{-1}$ indicating multiple size regimes. After 9 h, the average particle size has decreased, although there are still two distinct size regimes. Fig. 5(b) shows there is a rapid decrease in the characteristic length-scale r_g over the first half hour. The rate of change decreases between 30 min and 2 h, at which point r_g increases, possibly due to moisture assisted reorientation of grain boundaries and consolidation of smaller particles. In Fig. 5(c), we see the right, and downwards shift of the broad CsFAMAX peak (q∼0.017 $Å^{-1}$) initially centred on q∼0.0165 $Å^{-1}$ to ∼0.0175 $Å^{-1}$ which indicates the gradual formation of deuterated perovskite (CsFAMAX•D_2O; q∼0.0177 $Å^{-1}$). In particular, the slight shoulder at q∼0.021 $Å^{-1}$ suggests formation of FAMAX or $FAPbI_3$ mono-deuterates. Overall this film is distinguished by remarkably little phase segregation over the course of the measurements, which is in agreement with other research showing the enhanced moisture stability of this mixed A-site cation perovskite [15,41]. The intensity of scattering from the peak reduces, suggesting reduced structural order. It is unclear why there is an initial decrease in intensity between 1-2 h, followed by an increase at 3 h, and a final decrease by 9 h. It is possible the initial decrease in r_g is followed by moisture facilitated grain growth between 2-3 h, increasing average particle size and hence r_g. After deuteration particles follow a normal logarithmic distribution of sizes as shown in the histogram in Fig. 5(d). Comparison of SEM before (Fig. 5(e)) and after (Fig. 5(f)) hydration shows that average particle size reduces by approximately 50%. While grains which do not degrade do not show much change in size, those which do decompose to crystallite clusters orders of magnitude

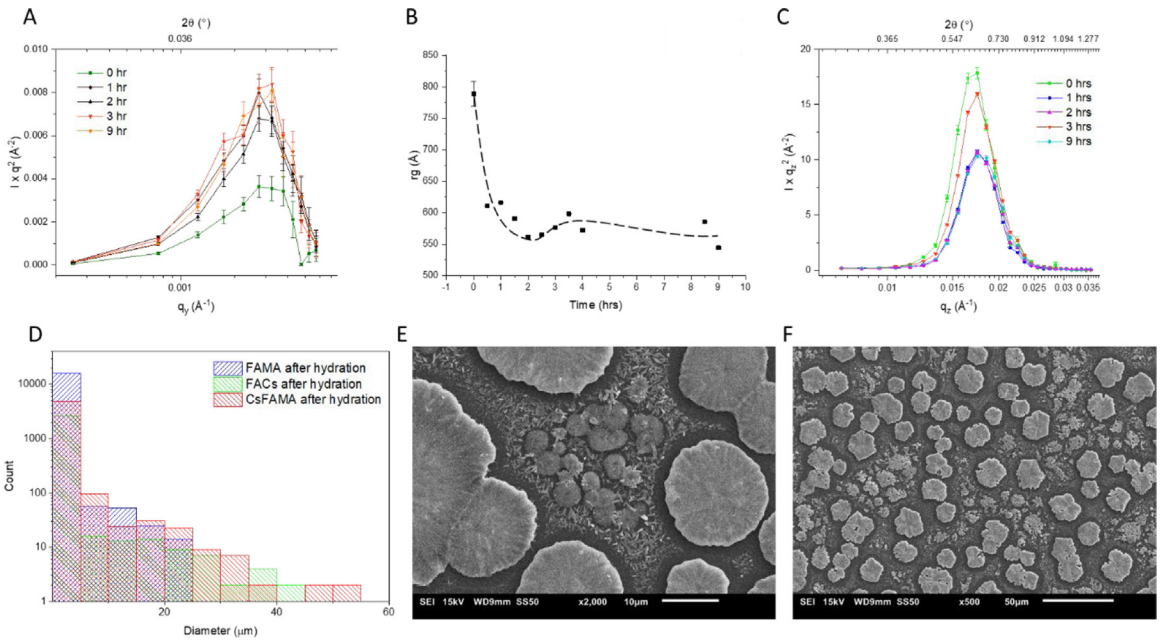

Fig. 5. A, C; Kratky Plots of CsFAMAX; Temporal data incomplete due to limitations in data reduction. (A) Horizontal Cut at 3.8 Åof CsFAMAX showing increasing scattering intensity from the lateral features at the surface. (B) Guinier model fit of horizontal scattering cut at 3.8 Å as per A, showing steep initial drop off in characteristic length-scale r_g at the surface. (C) Vertical cut at 3.8 Å showing shift of peak centre to higher q and lower intensity. (D) Particle size distribution after hydration. (E–F) SEM images at Mx500 and Mx2000 of CsFAMAX after 8 h hydration.

smaller. Across all three A-site alloyed samples, moisture induced degradation results in decreasing average particle size as perovskite grains swell and fragment from the grain periphery moving inwards.

5. Conclusion

In the datasets as the angular range increases above $q = 0.02$-0.03 Å, diffraction features come to dominate the scattering pattern. Error bars become larger due to low flux and hence these peaks become less reliable. This is exacerbated for cuts through scattering from an incident beam of 3.8 Å (3.8–4.2 Å wave-band) due to the lower scattering volume in this geometry (sampling along the surface). These could be corroborated with dedicated wide-angle neutron scattering experiment or neutron diffraction. The similar values for θ_c of several phases – particularly the deuterates – also makes it difficult to differentiate between them, and this would be further motivation to compliment this work with further neutron diffraction experiments. The high relative humidity of 90% may not be representative of typical operating conditions for these perovskite films when encapsulated in modules, but this experiment can be seen as a greatly accelerated simulation of the degradation processes which gradually occur over longer timescales. Average relative humidity ranges can readily reach 90% in a country with similar climate to the UK. Schlipf et al. found that the trend of water uptake exhibits a plateau between 30% rH and 60% rH attributed to crystal surfaces becoming saturated with adsorbed water [13]. At higher humidities, this water is incorporated into the crystal and hydrates form. Tolouenia et al. using dark pulse discharge measurements similarly found that at 60% rH there is no penetration of water into perovskite film whereas at 100% rH the number of ionic species increases with the formation of PbI_2 and aqueous MAI [39]. In this work we show that at 90% rH in the dark degradation of mixed A-site cation perovskite films proceeds through a process of degradation from the grain peripheries inwards. The film bulk shows a more rapid decline in characteristic scattering length than the film surface, which agrees with theories that degradation is initiated in the bulk. Moisture first adsorbs to the film along grain boundaries before permeating inside the grains and beginning a gradual process of decomposition from the outside in. Across all films we find evidence for the formation of deuterated degradation products, although reduction of the Methylammonium

component and substitution with Cs is particularly beneficial for moisture resistance, ensuring the preservation of larger grains, reduced perovskite phase segregation and reduced production of photo-inactive lead halide species.

Overall we reiterate that it is important to develop methods of mitigating degradation of the photoactive component of solar cells. Improving our understanding of how they fail will help us develop strategies to prevent this or slow it down, using additives, interfacial layers or better processing and synthesis. Our experiment demonstrates that multi-cation, multi-halide alloying of perovskites is an effective way of reducing the segregation of mixed perovskites into their component crystals. However morphological degradation leading to discontinuous smaller grains and longer grain boundaries is still observed under high humidity, and developing effective methods of reducing grain boundary mobility, moisture ingress, and hydrophilicity are sorely needed. TOF-GISANS is demonstrated as a potent and vital technique in the arsenal of material scientists seeking to characterise compounds containing organic moieties and understanding moisture induced degradation.

Funding sources

This work was funded by the UK Engineering and Physical Sciences Research Council (EPSRC) via a Ph.D. studentship for A.U. at the University of Sheffield from the Centre for Doctoral Training in New and Sustainable Photovoltaics, grant code EP/L01551X/2, which K.T. and F.B. also acknowledge for funding.

Declaration of competing interest

The authors declare that they have no known competing financial interests or personal relationships that could have appeared to influence the work reported in this paper.

Acknowledgements

Experiments at the ISIS Pulsed Neutron and Muon Source were supported by a beamtime allocation from the Science and Technology Facilities Council. We also gratefully acknowledge Sarah Rodgers for her assistance on the Sans2d *Time-of-flight Small-Angle Neutron Scattering instrument.*

This work benefited from the use of the SasView application, originally developed under NSF, UK award DMR-0520547. SasView contains code developed with funding from the European Union's Horizon 2020 research and innovation programme under the SINE2020 project, grant agreement No. 654000. See other publications and documentation concerning SasView at http://www.SasView.org/.

References

[1] Boyd CC, Cheacharoen R, Leijtens T, McGehee MD. Understanding degradation mechanisms and improving stability of perovskite photovoltaics. Chem Rev 2019;119:3418–51. http://dx.doi.org/10.1021/acs.chemrev.8b00336.

[2] Divitini G, Cacovich S, Matteocci F, Cinà L, Carlo ADi, Ducati C. In situ observation of heat-induced degradation of perovskite solar cells. Nat Energy 2016;1(15012). http://dx.doi.org/10.1038/NENERGY.2015.12.

[3] Leijtens T, Hoke ET, Grancini G, Slotcavage DJ, Eperon GE, Ball JM, et al. Mapping electric field-induced switchable poling and structural degradation in hybrid lead halide perovskite thin films. Adv Energy Mater 2015;5:1500962. http://dx.doi.org/10.1002/aenm.201500962.

[4] Frost JM, Butler KT, Brivio F, Hendon CH, Schilfgaarde MVan, Walsh A. Atomistic origins of high-performance in hybrid halide perovskite solar cells. Nano Lett 2014;14:2584–90. http://dx.doi.org/10.1021/nl500390f.

[5] Liao WC, Liu BH, Leu CC. Nanoscale mapping of humid degradation-induced local mechanical property variation in CH3NH3PbI3 polycrystalline film by scanning probe microscopy. Appl Surf Sci 2020;507:145078. http://dx.doi.org/10.1016/j.apsusc.2019.145078.

[6] Wang Q, Chen B, Liu Y, Deng Y, Bai Y, Dong Q, et al. Scaling behavior of moisture-induced grain degradation in polycrystalline hybrid perovskite thin films. Energy Environ Sci 2017;10:516–22. http://dx.doi.org/10.1039/C6EE02941H.

[7] Chen Solanki, Pan Sum. Compositional and morphological changes in water-induced early-stage degradation in lead halide perovskites. Coatings 2019;9(535). http://dx.doi.org/10.3390/coatings9090535.

[8] Leguy AMA, Hu Y, Campoy-Quiles M, Alonso MI, Weber OJ, Azarhoosh P, et al. Reversible hydration of CH3NH3PbI3 in films, single crystals, and solar cells. Chem Mater 2015;27:3397–407. http://dx.doi.org/10.1021/acs.chemmater.5b00660.

[9] Petrus ML, Hu Y, Moia D, Calado P, Leguy AMA, Barnes PRF, et al. The influence of water vapor on the stability and processing of hybrid perovskite solar cells made from non-stoichiometric precursor mixtures. ChemSusChem 2016;9:2699–707. http://dx.doi.org/10.1002/cssc.201600999.

[10] Schelhas LT, Li Z, Christians JA, Goyal A, Kairys P, Harvey SP, et al. Insights into operational stability and processing of halide perovskite active layers. Energy Environ Sci 2019;12:1341–8. http://dx.doi.org/10.1039/c8ee03051k.

[11] Yang J, Siempelkamp BD, Liu D, Kelly TL. Investigation of CH 3 NH 3 PbI 3 degradation rates and mechanisms in controlled humidity environments using in situ techniques. ACS Nano 2015;9:1955–63. http://dx.doi.org/10.1021/nn506864k.
[12] Noh JH, Im SH, Heo JH, Mandal TN, Seok S Il. Chemical management for colorful, efficient, and stable inorganic-organic hybrid nanostructured solar cells. Nano Lett 2013;13:1764–9. http://dx.doi.org/10.1021/nl400349b.
[13] Schlipf J, Bießmann L, Oesinghaus L, Berger E, Metwalli E, Lercher JA, et al. In situ monitoring the uptake of moisture into hybrid perovskite thin films. J Phys Chem Lett 2018;9:2015–21. http://dx.doi.org/10.1021/acs.jpclett.8b00687.
[14] Chu Z, Yang M, Schulz P, Wu D, Ma X, Seifert E, et al. Impact of grain boundaries on efficiency and stability of organic–inorganic trihalide perovskites. Nat Commun 2017;8:1–8. http://dx.doi.org/10.1038/s41467-017-02331-4.
[15] Lee JW, Kim DH, Kim HS, Seo SW, Cho SM, Park NG. Formamidinium and cesium hybridization for photo- and moisture-stable perovskite solar cell. Adv Energy Mater 2015;5. http://dx.doi.org/10.1002/aenm.201501310.
[16] Eperon GE, Stranks SD, Menelaou C, Johnston MB, Herz LM, Snaith HJ. Environmental science formamidinium lead trihalide A broadly tunable perovskite for Efficient planar heterojunction solar. 2014, p. 982–8. http://dx.doi.org/10.1039/c3ee43822h.
[17] Lee J, Seol D, Cho A, Park N. High-efficiency perovskite solar cells based on the black polymorph of HC(NH 2) 2 PbI 3. Adv Mater 2014;26:4991–8. http://dx.doi.org/10.1002/adma.201401137.
[18] Jeon NJ, Noh JH, Yang WS, Kim YC, Ryu S, Seo J, et al. Compositional engineering of perovskite materials for high-performance solar cells. Nature 2015;517:476–80. http://dx.doi.org/10.1038/nature14133.
[19] Beal RE, Slotcavage DJ, Leijtens T, Bowring AR, Belisle RA, Nguyen WH, et al. Cesium lead halide perovskites with improved stability for tandem solar cells. J Phys Chem Lett 2016;7:746–51. http://dx.doi.org/10.1021/acs.jpclett.6b00002.
[20] Li N, Tao S, Chen Y, Niu X, Onwudinanti CK, Hu C, et al. Cation and anion immobilization through chemical bonding enhancement with fluorides for stable halide perovskite solar cells. Nat Energy 2019;4:408–15. http://dx.doi.org/10.1038/s41560-019-0382-6.
[21] Tennyson EM, Roose B, Garrett JL, Gong C, Munday JN, Abate A, et al. Cesium-incorporated triple cation perovskites deliver fully reversible and stable nanoscale voltage response. ACS Nano 2018;13:1538–46. http://dx.doi.org/10.1021/acsnano.8b07295.
[22] Li Z, Yang M, Park J, Wei S, Berry JJ, Zhu K. Stabilizing perovskite structures by tuning tolerance factor: Formation of formamidinium and cesium lead iodide solid-state alloys 2. 2016, http://dx.doi.org/10.1021/acs.chemmater.5b04107.
[23] Yi C, Luo J, Meloni S, Boziki A, Ashari-Astani N, Grätzel C, et al. Entropic stabilization of mixed A-cation ABX3 metal halide perovskites for high performance perovskite solar cells. Energy Environ Sci 2016;9:656–62. http://dx.doi.org/10.1039/c5ee03255e.
[24] Ho K, Wei M, Sargent EH, Walker GC. Grain transformation and degradation mechanism of formamidinium and cesium lead iodide perovskite under humidity and light. ACS Energy Lett 2021;6:934–40. http://dx.doi.org/10.1021/acsenergylett.0c02247.
[25] Li N, Luo Y, Chen Z, Niu X, Zhang X, Lu J, et al. Microscopic degradation in formamidinium-cesium lead iodide perovskite solar cells under operational stressors. Joule 2020;4:1743–58. http://dx.doi.org/10.1016/j.joule.2020.06.005.
[26] Maniyarasu S, Ke JCR, Spencer BF, Walton AS, Thomas AG, Flavell WR. Role of alkali cations in stabilizing mixed-cation perovskites to thermal stress and moisture conditions. ACS Appl Mater Interfaces 2021. http://dx.doi.org/10.1021/acsami.1c10420.
[27] Hu Y, Aygüler MF, Petrus ML, Bein T, Docampo P. Impact of rubidium and cesium cations on the moisture stability of multiple-cation mixed-halide perovskites. ACS Energy Lett 2017;2:2212–8. http://dx.doi.org/10.1021/acsenergylett.7b00731.
[28] Wolff M, Herbel J, Adlmann F, Dennison AJC, Liesche G, Gutfreund P, et al. Depth-resolved grazing-incidence time-of-flight neutron scattering from a solid–liquid interface. J Appl Crystallogr 2014;47:130–5. http://dx.doi.org/10.1107/S1600576713028665.
[29] Gong J, Guo P, Benjamin SE, Van Patten PG, Schaller RD, Xu T. Cation engineering on lead iodide perovskites for stable and high-performance photovoltaic applications. J Energy Chem 2018;27:1017–39. http://dx.doi.org/10.1016/j.jechem.2017.12.005.
[30] Saliba M, Matsui T, Seo J-Y, Domanski K, Correa-Baena J-P, Nazeeruddin MK, et al. Cesium-containing triple cation perovskite solar cells: improved stability, reproducibility and high efficiency. Energy Environ Sci 2016;9:1989–97. http://dx.doi.org/10.1039/C5EE03874J.
[31] Hexemer A, Müller-Buschbaum P. Advanced grazing-incidence techniques for modern soft-matter materials analysis. IUCrJ 2015;2:106–25. http://dx.doi.org/10.1107/S2052252514024178.
[32] Müller-Buschbaum P. Grazing incidence small-angle neutron scattering: Challenges and possibilities. Polym J 2013;45:34–42. http://dx.doi.org/10.1038/pj.2012.190.
[33] Nouhi S, Hellsing MS, Kapaklis V, Rennie AR. Grazing-incidence small-angle neutron scattering from structures below an interface. J Appl Crystallogr 2017;50:1066–74. http://dx.doi.org/10.1107/S1600576717007518.
[34] Lee SW, Kim S, Bae S, Cho K, Chung T, Mundt LE, et al. UV degradation and recovery of perovskite solar cells. Sci Rep 2016;6:1–10. http://dx.doi.org/10.1038/srep38150.
[35] Young JF. Humidity control in the laboratory using salt solutions-a review. J Appl Chem 2007;17:241–5. http://dx.doi.org/10.1002/jctb.5010170901.
[36] Schneider CA, Rasband WS, Eliceiri KW, Instrumentation C. NIH image to ImageJ 25 years of image analysis 9. 2017, p. 671–5.
[37] Fransishyn KM, Kundu S, Kelly TL. Elucidating the failure mechanisms of perovskite solar cells in humid environments using in situ grazing-incidence wide-angle X-ray scattering. ACS Energy Lett 2018;3:2127–33. http://dx.doi.org/10.1021/acsenergylett.8b01300.
[38] Hada M, M. Abdullah Al Asad, Misawa M, Hasegawa Y, Nagaoka R, Suzuki H, et al. A mechanistic investigation of moisture-induced degradation of methylammonium lead iodide. Appl Phys Lett 2020;117. http://dx.doi.org/10.1063/5.0021338.
[39] Tolouеinia P, Khassaf H, Amin AShirazi, Tobin ZM, Alpay SP, Suib SL. Moisture-induced structural degradation in methylammonium lead iodide perovskite thin films. ACS Appl Energy Mater 2020;3:8240–8. http://dx.doi.org/10.1021/acsaem.0c00638.
[40] Mcgovern L, Futscher MH, Muscarella LA, Ehrler B. Understanding the stability of mapbbr 3 versus mapbi 3 : Suppression of methylammonium migration and reduction of halide migration. 2020, http://dx.doi.org/10.1021/acs.jpclett.0c01822.
[41] Liu Y, Wu Z, Dou Y, Zhang J, Bu T, Zhang K, et al. Formamidinium-based perovskite solar cells with enhanced moisture stability and performance via confined pressure annealing. J Phys Chem C 2020;124:12249–58. http://dx.doi.org/10.1021/acs.jpcc.0c02289.